

Contents lists available at ScienceDirect

# Thin Solid Films

journal homepage: www.elsevier.com/locate/tsf





# Effects of atmosphere composition during direct ultraviolet-light patterning of solution-deposited In<sub>2</sub>O<sub>3</sub> thin film transistors

Trey B. Daunis<sup>+</sup>, Weijie Xu<sup>+</sup>, Sampreetha Thampy, Marisol Valdez, Julia W.P. Hsu<sup>+</sup>

Department of Materials Science and Engineering, University of Texas at Dallas, 800 W Campbell Rd, Richardson, TX 75080, USA

#### ARTICLE INFO

Keyword: UV exposure Atmospheric effect Sol-gel Metal oxide Thin film transistors

#### ABSTRACT

Sol-gel synthesis is widely used to fabricate metal oxide thin films by solution, but it requires high-temperature thermal annealing to fully convert precursors to metal oxides. Exposure to Ultraviolet (UV) light before thermal annealing of precursor films has been shown to reduce the conversion temperature, with the added benefits of film patterning when done through a shadow mask and improved device performance. However, the mechanism by which UV exposure under different atmospheric compositions affects the properties of metal oxide films after thermal annealing has not been investigated. Here, we control the atmospheric composition during UV-patter $ning\_prior\ to\ high-temperature\ thermal\ annealing\_of\ In_2O_3\ sol-gel\ films\ which\ serve\ as\ the\ semiconductor\ in$ thin-film transistors. Despite all films being annealed at 250°C in air after UV patterning, films exposed to UV under oxygen-containing atmospheres have higher metal-oxygen-metal bonding and exhibit higher transistor mobility compared to the films exposed to UV under N2 atmosphere. The origin of the effect of atmospheric composition on mobility is studied through X-ray photoelectron spectroscopy (XPS) and Fourier-transform infrared spectroscopy and is revealed to be the result of the reformation of the nitrate species in the films under more oxidizing atmospheres during UV exposure. These nitrates can be completely removed by thermal annealing, facilitating more complete metal-oxygen-metal bond formation, which is reflected in higher O<sub>I</sub> XPS signal and transistor mobility. In contrast, films processed under N2 atmosphere during UV exposure contain nitrite species that cannot be removed by thermal annealing, resulting in less metal-oxygen-metal bond formation and lower mobility.

# 1. Introduction

Metal oxides are ideal materials for many thin-film electronic applications due to their greater long-term stability compared to organics and their wide variety of electronic properties including dielectric, semiconducting, ferroelectric, and transparent conducting behaviors [1, 2]. Sol-gel chemistry is widely used for the fabrication of metal oxide films by solution [3]. A high-temperature, typically > 400°C, thermal annealing step is needed to convert the sol-gel precursors to metal oxides. Recent interest in using metal oxide films for flexible electronics drives the need to lower the processing temperature to be compatible with plastic substrates [4,5]. It was shown that exposing sol-gel precursor films to ultraviolet (UV) light prior to thermal annealing is effective in lowering the conversion temperature while producing good device performance [6–9]. When performed through a shadow mask, patterned films are produced due to selective conversion of the UV

exposed areas; subsequent rinsing in a developing solution removes the precursor in the unexposed regions [10–12]. Additionally, it has been reported that UV exposure prior to thermal annealing improves the properties of the annealed oxide film compared to thermal annealing only without UV treatment [8,13].

The effect of UV irradiation on the conversion of metal-nitrate precursors to metal oxides is currently understood to be due to the generation of oxygen-radical species through the photolytic decomposition of nitrate ions [9,14,15]. This decomposition pathway involves multiple reactive oxygen species and results in the formation of metal-oxygen-metal (M-O-M) bonds. UV exposure alone is not sufficient to fully convert sol-gel precursor films to metal oxides and additional thermal annealing is needed [10]. Furthermore, while some studies perform the UV exposure in an  $N_2$  atmosphere [7,16,17] or prevent oxygen and UV-generated ozone from contacting the sample by using a hard contact quartz photomask during UV patterning [12], other studies

E-mail address: jwhsu@utdallas.edu (J.W.P. Hsu).

<sup>\*</sup> Corresponding author.

<sup>&</sup>lt;sup>+</sup> These authors contributed equally.

perform UV exposure in air in the presence of both atmospheric oxygen and UV-generated ozone [18–20]. While successful patterning was reported in these publications, how UV exposure under different atmospheres affects the properties of fully converted metal oxide films after thermal annealing, and the mechanism by which this occurs, has not been investigated.

Here, we control the atmospheric composition during UV patterning of solution-deposited  $\rm In_2O_3$  sol-gel films prior to  $250^{\circ}\rm C$  thermal annealing. The atmospheric effects on the chemical properties of the final oxide films and thin-film transistor (TFT) devices are examined and elucidated. The chemical properties of the films after UV exposure and after thermal annealing are evaluated through X-ray photoelectron spectroscopy (XPS) and Fourier-transform infrared (FTIR) spectroscopy. Since many oxide semiconductors and dielectrics have been processed using similar methods, our study of  $\rm In_2O_3$  can be applied to other binary oxides made from nitrate precursors [21,22].

# 2. Experimental details

#### 2.1. In<sub>2</sub>O<sub>3</sub> Precursor Film Deposition

The  $\rm In_2O_3$  precursor solution was prepared by dissolving 0.1M In  $(\rm NO_3)_3\bullet 3\rm H_2O$  in 2-methoxyethanol, followed by the addition of 0.1M NH<sub>4</sub>OH and 0.1M acetylacetone. The solution was stirred at room temperature for 48 h prior to film deposition. The resulting solution strongly absorbs UV light with a wavelength < 320 nm [10]. Gold-coated p<sup>++</sup> silicon substrates for XPS, undoped (intrinsic) silicon substrates for FTIR, and p<sup>++</sup> silicon wafers with 177 nm thermally grown SiO<sub>2</sub> (measured by ellipsometry, J.A. Woollam M2000DI) for TFTs were rinsed in acetone, isopropyl alcohol, and deionized water (DI) water followed by UV-ozone treatment (Bioforce Nanosciences Procleaner Plus) for 20 min prior to  $\rm In_2O_3$  deposition. The  $\rm In_2O_3$  precursor solution was spin coated onto the prepared substrates at 3,000 rpm for 30 s, and the samples were immediately dried on a hotplate at 80°C for 3 min. The thickness of the precursor film is ~28 nm [10].

# 2.2. Patterning Treatment and Annealing

Prior to 250°C thermal annealing, dried precursor films were treated by one of four methods in the UV-ozone apparatus (Samco model UV-1): ozone (O<sub>3</sub>) only, UV in a nitrogen atmosphere (UV-N<sub>2</sub>), and UV with ozone generated both in-situ from the air by the UV radiation (UV-Air) and ex-situ in an ozone generator (UV-O3). Samples for TFTs first had a 0.005" thick invar shadow mask placed on top which was held in place by a magnet on the bottom of the sample. Samples for XPS and FTIR analysis were treated without a mask but were placed on top of the same magnets to ensure the same distance between the sample and UV light source. For O<sub>3</sub>-only and UV-O<sub>3</sub>, oxygen was flowed through the external ozone generator at 0.5 L per min (lpm) and then into the sample chamber without (O3-only) or with (UV-O3) the low-pressure mercury UV lamp (254 nm and 185 nm radiation) turned on. For UV-N2, the chamber was purged with N<sub>2</sub> at 3 lpm for 5 minutes prior to exposure to UV, and the chamber was continuously purged with N2 during UV exposure. For UV-Air, samples were processed without purging by closing the chamber and turning on the UV lamp. Samples were exposed to UV for 10 min. Patterning experiments were performed at 90°C to avoid an increase in temperature from the UV light during exposure. Following the treatment, the shadow masks were removed and the samples were dipped into a developing solution (15 mL DI water, 5 mL methanol, and 1 mL acetic acid) for 5 s to remove the unexposed precursor film followed by a thorough rinse in DI water. All patterned films were then annealed on a hotplate at 250°C in air for 20 min. The film thickness differs by less than 10% for the three atmospheric compositions: ~13 nm after UV exposure and ~7 nm after thermal annealing, which is not affected by the developing solution [10]. The complete process for deposition of In<sub>2</sub>O<sub>3</sub> films is shown schematically in Fig. 1.

# 2.3. X-ray Photoelectron Spectroscopy

XPS was performed on a Ulvac-PHI VersaProbe2 with a monochromated Al Ka source (1486.8 eV) at an angle of  $45^{\circ}$  to the sample surface at 50 W and 15 kV with a 200  $\mu$ m beam size. Scanning was performed with an energy step of 0.2 eV at 20 ms per step and a pass energy of 23.5 eV. All spectra are averaged over 20 scans. XPS data were

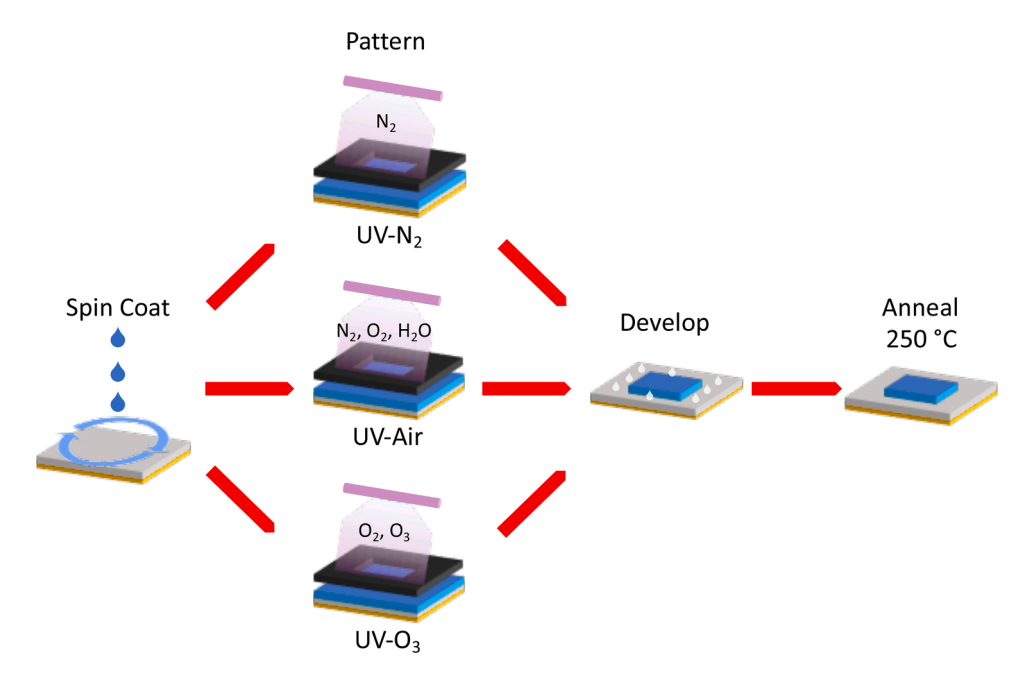


Fig. 1. Schematics of  $In_2O_3$  film processing. From left to right,  $In_2O_3$  sol-gel precursor is spin coated on a  $Si/SiO_2$  substrate and the dried film is exposed through a shadow mask to a UV lamp in nitrogen (UV-N<sub>2</sub>, top), air (UV-Air, middle), or ozone (UV-O<sub>3</sub>, bottom) atmosphere. The samples are rinsed in a developing solution to remove the unexposed areas and are annealed on a hotplate at  $250^{\circ}$ C in air for 20 min.

analyzed using commercial software (MultiPak, Ulvac-PHI).

# 2.4. Fourier-Transform Infrared Spectroscopy

FTIR measurements were performed in a Nicolet iS50 spectrometer with a mercury cadmium telluride (MCT-A) detector under  $N_2$  purge. All spectra were collected with a resolution of 4 cm $^{-1}$  in the range of 650–4000 cm $^{-1}$ . The sample spectra were referenced to the spectra of the bare intrinsic silicon substrates, and residual water vapor absorption signals were removed by subtraction.

# 2.5. Spectroscopy Ellipsometry

Spectroscopic ellipsometry measurements (M-2000DI, J. A. Woolam) at  $55^{\circ}$ ,  $65^{\circ}$ , and  $75^{\circ}$  incident angles from 300 to 1690 nm in wavelength were done to determine the thickness and optical constants of films. The fitting was performed using a Cauchy model between 600 and 1690 nm.

# 2.6. Atomic Force Microscopy

Film roughness was measured using an atomic force microscope (Asylum MFP-3D). 5  $\mu$ m x 5  $\mu$ m Atomic Force Microscope (AFM) images were taken at three different locations.

#### 2.7. Transistor Fabrication and Measurements

To finish the transistors, 100 nm Al source and drain contacts were deposited by thermal evaporation through a shadow mask to define a channel with a width of 1,000  $\mu m$  and length of 100  $\mu m$ . Metal-insulator-metal capacitors were defined by 400  $\mu m$  x 400  $\mu m$  Al top contacts in regions where the  $\rm In_2O_3$  was removed by the patterning process, and the capacitance of the gate dielectric, used in calculating the channel mobility, was measured using an Agilent 4284A Precision LCR Meter at 10 kHz with 0 V DC bias and 50 mV AC amplitude. Transfer output curves were measured in a Keithley 4200-SCS Semiconductor Characterization System with drain voltage at 35 V for transfer curve measurements to ensure saturation operation of the transistors.

# 3. Results and discussion

When performing patterning using UV in air [10,19,20], partial conversion of metal oxide films can be due to exposure to the high energy of UV light, the reactive oxygen atmosphere, or both. To separate the contributions from these effects, we first exposed In<sub>2</sub>O<sub>3</sub> precursor films to ozone only (O3-only) or UV only with no ozone or oxygen (UV-N<sub>2</sub>) to determine whether reactive oxygen species or UV light is the necessary component for film patterning. Films exposed to O3-only showed no chemical resistance to the developing solution even after one hour of exposure. The entire film, in both exposed and unexposed regions, was removed by the developing solution. However, films exposed to UV light only (UV-N<sub>2</sub>) for just 10 min showed excellent contrast after developing, with the exposed regions remaining on the substrate. Thus, UV is the necessary component responsible for the initiation of metal oxide conversion. Exposure to mercury vapor lamp emission through glass optics that blocks the shorter wavelength UV light was also found to produce no patterns, suggesting that it is the strong emissions at 185 nm and/or 254 nm which are responsible for conversion. Our result confirms previous reports that suggest the decomposition of nitrates induced by UV photons [9,23]. While we show that ozone alone is not enough to initiate conversion to metal oxide, we are curious whether the presence of ozone in combination with UV during patterning has a positive or negative effect: on one hand, oxygen and ozone can absorb UV light and reduce UV intensity delivered to the sample, but on the other hand, reactive oxygen species were proposed to facilitate M-O-M bond formation and film densification [24,25]. To examine these effects, we prepared films under three different atmospheric conditions: UV-N2,

UV-Air, and UV- $O_3$ , as shown in the second step in Fig. 1. The four-step process depicted in Fig. 1 consists of depositing the sol-gel precursor film, patterning with UV exposure under various atmospheric compositions, developing the pattern, and finally annealing the oxide film thermally.

## 3.1. Transistor Performance

Transistors were fabricated using a  $p^{++}$  silicon substrate as the back gate with a 177 nm thick thermal SiO<sub>2</sub> layer as the gate dielectric. Fig. 2a shows the transfer curves measured on devices with 250°C-annealed In<sub>2</sub>O<sub>3</sub> semiconductor layer but patterned under each of the three UV exposure atmospheres. Fig. 2b shows the drain current vs. drain voltage output characteristics of each device demonstrating saturation regime operation for the measurement conditions used in Fig. 2a. The field effect mobility ( $\mu_{FE}$ ) for each device was extracted using the saturated mobility equation:

$$\mu = \left(\frac{d\sqrt{I_D}}{dV_G}\right)^2 2\frac{L}{WC}$$

where  $I_D$  is the drain current,  $V_g$  is the gate voltage, L is the channel length, W is the channel width, and C is the areal gate capacitance. The values for  $\frac{d\sqrt{I_D}}{dV_G}$  were extracted from linear fits (thin solid lines) to the  $I_D^{1/2}$ vs. V<sub>G</sub> data (dashed lines) plotted on the right y-axis in Fig. 2a. While each type of device has a similar threshold voltage of  $\sim$  4 V, the UV-N<sub>2</sub> device (red) has the lowest mobility (1.9  $\pm$  0.5 cm<sup>2</sup> V<sup>-1</sup>s<sup>-1</sup>), followed by UV-Air (light blue,  $3.1 \pm 0.7$  cm<sup>2</sup> V<sup>-1</sup>s<sup>-1</sup>), and UV-O<sub>3</sub> (dark blue,  $4.4 \pm$  $0.7 \text{ cm}^2 \text{ V}^{-1} \text{s}^{-1}$ ) which has the highest mobility within one batch. Two more batches were made, and the mobility of at least 7 devices was examined to further confirm the statistical difference between the 3 conditions (Fig. 2c). As all devices were annealed at 250°C after the patterning step, the distinct mobility difference shows that the atmospheric composition during the UV patterning step is critical in determining the semiconductor films' eventual electrical properties, which cannot be erased even after thermal annealing. This is unexpected because the thermal annealing step involves both a significantly higher temperature (250°C vs. 90°C) and longer duration (20 vs. 10 min) than the patterning step, and it suggests that the chemical or morphological changes induced by the atmospheric composition during the initial patterning step either persist after thermal annealing or affect the thermal annealing process. We applied AFM to examine whether there are any morphological differences. The roughness of UV-N2, UV-air, and UV-O3 is 0.69  $\pm$  0.02, 0.74  $\pm$  0.01, and 0.70  $\pm$  0.04 nm, respectively. Their similarity suggests that morphological differences do not play a critical role here.

# 3.2. Metal-oxygen Bond Formation Probed by XPS

To examine the film chemistry associated with the varying atmospheric conditions during UV exposure and the potentially lasting effects, we performed XPS on each type of film after UV exposure and after the 250°C annealing step. In previously reported studies, oxide semiconductor films with a larger percentage of  $\rm O_I$  peak at  $\sim\!529.5$  eV (attributed to M-O-M bonding) in the O 1s XPS spectra show higher field effect mobilities [18,19]. Fig. 3 compares the O 1s region of the XPS spectra for the three UV exposure conditions. Each O 1s peak is deconvoluted into three Gaussian peaks,  $\rm O_I$  at  $\sim\!532.5$  eV (blue curves),  $\rm O_{II}$  at  $\sim\!531.5$  eV (green curves), and  $\rm O_{III}$  at  $\sim\!532.5$  eV (orange curves). The shape of these peaks (full-width half-max and percent Gaussian characteristic) were fixed between the fitting for all samples, with the position and height allowed to vary.

Previously we showed that UV exposure increases the  $O_I$  contribution in the O 1s peak, consistent with M-O-M formation in the precursor films that make them resistant to developing solution [10]. Here we further show that the  $O_I$  contribution depends on the atmospheric

T.B. Daunis et al. Thin Solid Films 733 (2021) 138829

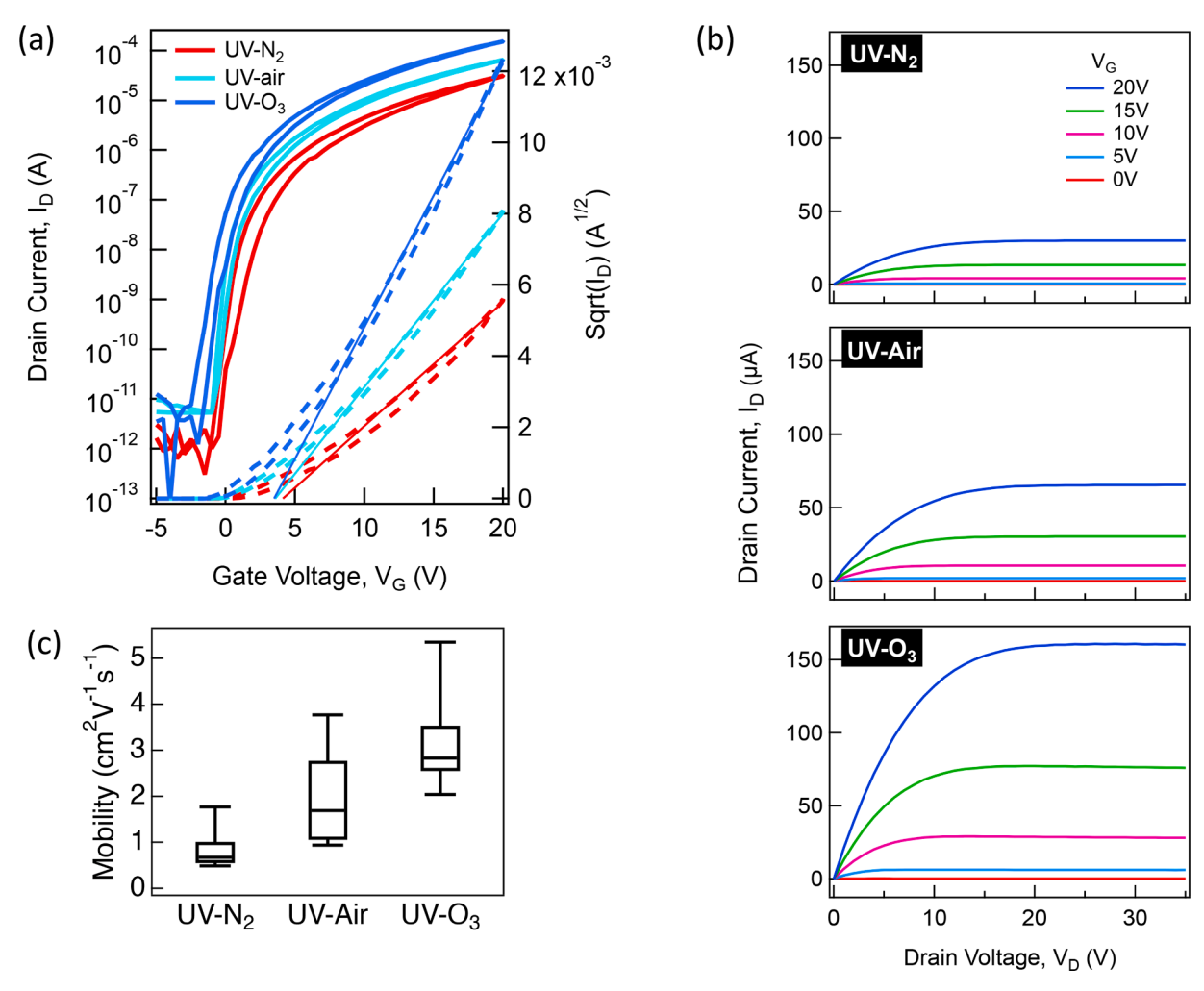


Fig. 2. TFT performance for  $In_2O_3$  transistors on  $Si/SiO_2$  substrates. (a) Transfer curves for  $In_2O_3$  patterned using  $UV-N_2$  (red), UV-Air (light blue), and  $UV-O_3$  (dark blue). A linear fit (thin solid lines) of the forward scan of  $I_0^{1/2}$  (dashed lines, right axis) in the linear region from 10 V to 20 V is used for the calculation of mobility.  $V_D$  is 35 V. (b) Output curves for  $In_2O_3$  patterned using  $UV-N_2$  (top), UV-Air (middle), and  $UV-O_3$  (bottom) showing saturation operation of the transistors at the voltages used in the transfer curves. (c) Statistical analysis of TFT mobility on at least 7 devices.

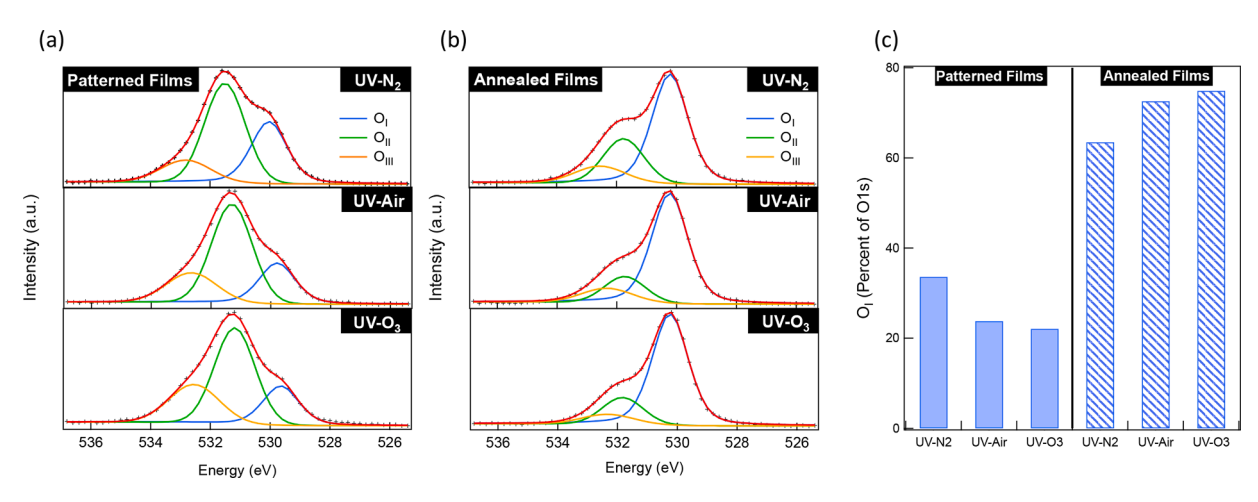


Fig. 3. O 1s XPS spectra. (a) Films patterned using UV-N<sub>2</sub> (top), UV-Air (middle), and UV-O<sub>3</sub> (bottom). (b) Films from (a) after annealing at  $250^{\circ}$ C in air. O 1 s peaks (measured data shown with black crosses, fitting with red curves) are deconvoluted into three peaks: O<sub>I</sub> (blue curves) at  $\sim 529.5$  eV, O<sub>II</sub> (green curves) at  $\sim 531.5$  eV, and O<sub>III</sub> (orange curves) at  $\sim 532.5$  eV. (c) Area under the O<sub>I</sub> peak as a percent of total O 1s area for each plot in (a) and (b). Solid bars represent patterned films and hashed bars represent thermally annealed films.

T.B. Daunis et al. Thin Solid Films 733 (2021) 138829

composition during UV exposure. Fig. 3a shows that after UV exposure (termed "patterned films"), the O<sub>I</sub> peak contributes to a significantly larger percentage of the O 1s signal for the UV-N2 sample compared to the two samples exposed to oxygen-containing atmospheres, and has the smallest contribution for the UV-O3 sample. After 250°C thermal annealing in air (termed "annealed films"), the OI peak contribution increases drastically and becomes the dominant component in the O 1s region for all samples (Fig. 3b), confirming that high-temperature thermal annealing is needed to fully convert the samples to metal oxides. However, the trend of relative OI peak contribution for the annealed films is opposite to that for the patterned films, with the UV-O  $_3$ sample exhibiting the largest percentage of the O<sub>I</sub> peak. Fig. 3c shows the area under the O<sub>I</sub> peak as a percentage of the total O 1s peaks for the UV-exposed films made under each condition (solid bars) and for the annealed films (hashed bars). In a simplistic mechanism in which the UV patterning process initiates M-O-M bonding and the thermal annealing process further completes the bond formation, the expected outcome is for both the patterned and annealed films to exhibit the same trend in the O<sub>I</sub> fraction, i.e., UV-N<sub>2</sub> > UV-Air > UV-O<sub>3</sub>, or for the O<sub>I</sub> peak areas to become equal for all methods after thermal annealing if thermal annealing erased the previous processing history. However, the experimental results show a reverse trend, i.e., O<sub>I</sub> fraction increases as UV-N<sub>2</sub> < UV-Air < UV-O<sub>3</sub> after thermal annealing. This surprising result signals that additional and lasting changes are produced by the atmospheric composition during the UV patterning, which affects the final thermal-annealing outcome. We note that the extent of M-O-M bonding (percent O<sub>I</sub> in O 1s) of the annealed films is consistent with the performance of the transistors: the UV-O3 device has the highest mobility and the largest extent of M-O-M bonding while the UV-N2 device has the lowest mobility and the smallest extent of M-O-M bonding.

# 3.3. Evolution of Nitrogen Species

As decomposition of nitrates is thought to be the first step in conversion from sol-gel precursors containing metal nitrates to metal oxide films during UV exposure [9], we compare the N 1s region of the XPS spectra and the NO<sub>x</sub> region from FTIR for each type of film after UV exposure (patterned films) and after thermal annealing in air (annealed films). The N 1s region for all patterned films (Fig. 4a, solid lines) shows two peaks centered at around 407 eV and 404 eV corresponding to nitrate  $(NO_3^-)$  and nitrite  $(NO_2^-)$  ions, respectively [21]. This indicates that the NO<sub>3</sub> precursor is not fully decomposed during UV exposure regardless of the atmospheric composition. However, the UV-N2 patterned film (top, red solid) shows a NO<sub>2</sub> peak with intensity slightly larger than the NO<sub>3</sub> peaks, while the UV-Air (middle, light blue solid) and UV-O<sub>3</sub> (bottom, dark blue solid) patterned films show a large NO<sub>3</sub> peak and a negligible NO<sub>2</sub> peak. While NO<sub>3</sub> is present in the precursor solution, NO2 is not, and thus must be generated during the UV exposure. After 250°C annealing (dashed lines), no NO<sub>3</sub> signal is observed in any of the films, but the NO<sub>2</sub> signal in UV-N<sub>2</sub> film remains.

To further corroborate the XPS results, we present the FTIR spectra of UV-N $_2$  (top, red), UV-Air (middle, light blue), and UV-O $_3$  (bottom, dark blue) in Fig. 4b. The UV-N $_2$  patterned film (red solid line) shows a broad peak from between  $\sim\!1300~\text{cm}^{-1}$  and  $\sim\!1600~\text{cm}^{-1}$ , indicating the presence of NO $_3^-$ /NO $_2^-$  species in the sample and consistent with the XPS results. In contrast, UV-Air, and UV-O $_3$  patterned films (solid lines) show narrower peaks, from  $\sim\!1300~\text{cm}^{-1}$  to  $\sim\!1500~\text{cm}^{-1}$ . After annealing (dashed lines), there are no peaks in the 1300–1600 cm $^{-1}$  region in UV-Air and UV-O $_3$  films, but peaks are still present in the UV-N $_2$  film. From the XPS results, we know that NO $_3^-$  species are completely removed by thermal annealing in the UV-Air and UV-O $_3$  films; therefore, the difference spectra between the annealed and patterned films made under UV-Air and UV-O $_3$  conditions (Fig. 4c light blue and dark blue curves) reflect the characteristic vibrational frequencies associated with

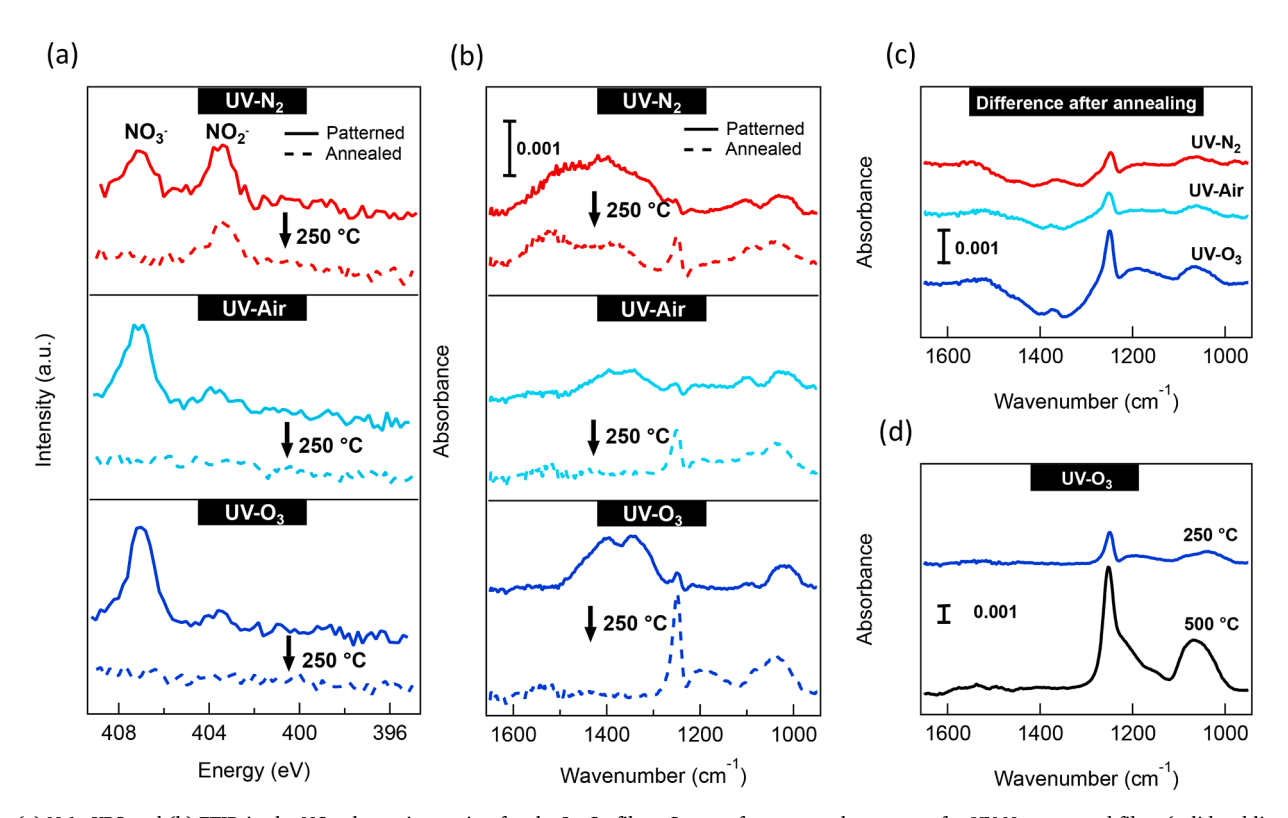


Fig. 4. (a) N 1s XPS and (b) FTIR in the  $NO_x$  absorption region for the  $In_2O_3$  films. Spectra from top to bottom are for  $UV-N_2$  patterned films (solid red lines) and annealed films (250°C, dashed red lines), UV-Air patterned (solid light blue lines) and annealed films (dashed light blue lines), and  $UV-O_3$  patterned (solid dark blue lines) and annealed films (dashed dark blue lines). (c) The difference FTIR spectra between patterned and annealed films from (b). (d) FTIR spectra for a  $UV-O_3$  film annealed at  $250^{\circ}C$  (blue) and  $500^{\circ}C$  (black), showing growth in the peaks centered at  $1250 \text{ cm}^{-1}$  and  $1030 \text{ cm}^{-1}$ .

T.B. Daunis et al. Thin Solid Films 733 (2021) 138829

 $NO_3^-$  species in these films. Note that the loss of FTIR signals in the annealed  $UV-N_2$  film (Fig. 4c red curve) is similar to the other two curves, indicating that  $NO_3^-$  species in this film are also removed by annealing. The remaining FTIR signals in the annealed  $UV-N_2$  film (Fig. 4b dashed red curve) must arise from the  $NO_2^-$  species, consistent with the XPS result (Fig. 4a, dashed red line). Our finding that  $NO_2^-$  species are not removed by thermal annealing is consistent with previous reports that  $NO_2^-$  species are more thermally stable compared to  $NO_3^-$  species [15,26].

Additionally, FTIR spectra of the patterned and especially annealed films show two peaks: at  $1250~\text{and}~1030~\text{cm}^{-1}$ . These peaks grow after annealing the  $\text{In}_2\text{O}_3$  films to  $250^\circ\text{C}$  (Fig. 4c). Further growth is observed upon annealing the UV-O $_3$  film to  $500^\circ\text{C}$  while all other absorption peaks are gone (Fig. 4d), which indicates that they are not from organic species. The intensity of these peaks correlates with the intensity of the O $_1$  peak in the O 1s XPS, suggesting that they arise from In-O vibrational modes in the oxide film. For silica glass made from sol-gel, the IR absorption peaks at 1220 and 1080 cm $^{-1}$  were assigned to the longitudinal optical (LO) and transverse optical (TO) modes of Si-O-Si asymmetric stretching [27]. Therefore, we postulate that the 1250 and 1030 cm $^{-1}$  peaks are due to the LO and TO modes of similar vibrations in the  $\text{In}_2\text{O}_3$  film.

# 3.4. Film Chemistry Due to Atmospheric Effect During UV Exposure on M-O-M Bond Formation Upon Thermal Annealing

Based on the XPS and FTIR results, we can now explain the observed differences in the M-O-M bond formation in the patterned and annealed films, as summarized by the reaction schematics in Fig. 5.

From previous studies on nitrate photodecomposition mechanisms, it is well known that  $NO_3^-$  ions are excited by UV irradiation to  $ONOO^-$  ions which then decompose under continued UV irradiation into  $NO_2^-$  and an oxygen free radical (O $^{\bullet}$ ) (Fig. 5, step ii-a/b) [25,28–30]. The released oxygen then participates in M-O-M bond formation. Because the inert atmosphere does not absorb UV radiation while oxygen and ozone atmospheres do, the UV-N<sub>2</sub> film is exposed to a higher intensity of UV radiation than the UV-Air and UV-O<sub>3</sub> films. Therefore, the amount of  $NO_3^-$  that is photo-decomposed under the UV-Air and UV-O<sub>3</sub> processes is lower compared to that under the UV-N<sub>2</sub> atmosphere. This leads to the observation that in the patterned films, M-O-M bond formation, as indicated by the O 1s O<sub>1</sub> peak, decreases in the order of UV-N<sub>2</sub> > UV-Air > UV-O<sub>3</sub> (Fig. 3c, solid bars). Under an inert atmosphere,  $NO_2^-$  remains in the sample as evidenced in the N 1s XPS spectrum of the UV-N<sub>2</sub> film (Fig. 4a, red solid line). This is schematically shown in Fig. 5, step iii-a.

In contrast, in the presence of a strongly oxidizing atmosphere, the generated  $NO_2^-$  is readily oxidized back into  $NO_3^-$  (Fig. 5, step iii-b), explaining the minimal presence of  $NO_2^-$  signal and stronger  $NO_3^-$  signals in the N 1s XPS spectra of patterned films made under oxygen-containing atmospheres (Fig. 4a, solid light and dark blue lines).

Under 250°C annealing, not only does the NO<sub>3</sub> species undergo thermal decomposition releasing NO<sub>x</sub> gases and leaving behind oxygen in the lattice (Fig. 5, step iv-a/b), it also acts as an oxidizer in the solution combustion process to provide energy in the form of additional heat which improves M-O-M bond formation.[31] The trend of NO<sub>3</sub> signals observed in Fig. 4a correlates well with the observed O<sub>I</sub> in O 1s XPS after annealing (Figure 3c, hatched bars). Thus, the more NO<sub>3</sub> in the film after UV exposure, the more oxygen and heat is available upon its decomposition for bond formation. With a stronger bond strength [32] and greater thermal stability[26] than NO<sub>3</sub>, NO<sub>2</sub> remains in the final annealed UV-N2 film (Fig. 4a, red dashed line) as illustrated in Fig. 5, step iv-a. As a result, the UV-O3 annealed film has the highest M-O-M bonds while the low amount of NO<sub>3</sub> coupled with the presence of thermally stable NO<sub>2</sub> explains the low M-O-M bond formation in the annealed UV-N<sub>2</sub> film. Finally, the trend in the extent of M-O-M bonding of the annealed films is responsible for the trend in the mobility of the transistors, with more M-O-M bonding resulting in higher mobility.

# 4. Conclusions

The combined device performance and spectroscopic materials studies allow us to assess the effects of atmospheric composition during the UV exposure prior to high-temperature thermal annealing on the conversion sol-gel precursor films. Even though the final metal oxide conversion is performed by thermal annealing at a high temperature for a prolonged time, the atmospheric composition during the preceding UV-patterning step strongly affects the performance of In2O3 semiconductor films used as the channel in thin-film transistors. An atmosphere containing more reactive oxygen species produces a greater extent of M-O-M bonding in the oxide film after thermal annealing, and thus higher mobility, despite resulting in less UV radiation reaching the sample and less M-O-M bonding formed during UV exposure. This is because the oxidizing atmosphere reverts the photo-decomposed nitrites to nitrates. These nitrates are the source for M-O-M bond formation during subsequent thermal annealing and can be completely decomposed at a relatively lower temperature than nitrites. Thus, performing UV-patterning of sol-gel oxide films under excess oxygen and ozone is beneficial to device performance, and is preferred over performing this step in an inert atmosphere or to using a hard mask to isolate the sample

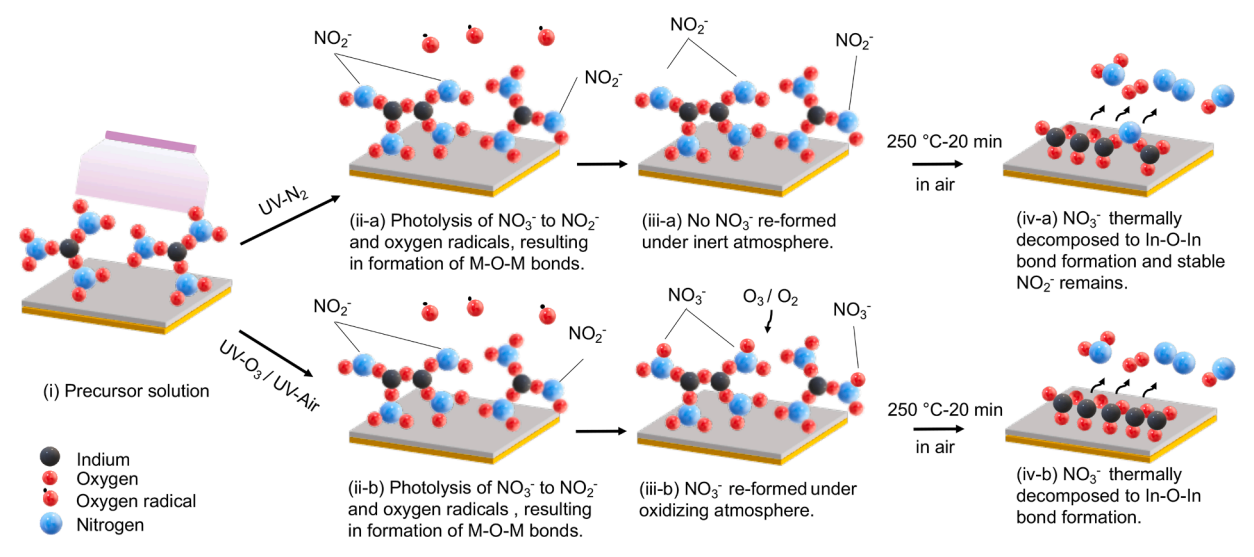


Fig. 5. Reaction schematics depicting the effects of UV exposure atmospheres on the films' chemical properties.

from ozone.

#### CRediT authorship contribution statement

**Trey B. Daunis:** Conceptualization, Methodology, Investigation, Validation, Data curation, Formal analysis, Writing – original draft. **Weijie Xu:** Conceptualization, Methodology, Investigation, Validation, Data curation, Formal analysis, Writing – original draft. **Sampreetha Thampy:** Formal analysis, Writing – review & editing. **Marisol Valdez:** Investigation, Data curation. **Julia W.P. Hsu:** Supervision, Methodology, Resources, Writing – review & editing.

# **Declaration of Competing Interest**

The authors declare that they have no known competing financial interests or personal relationships that could have appeared to influence the work reported in this paper.

# Acknowledgements

We thank J. Veyan for his help in the FTIR measurements and Prof. R. Wallace for the use of the spectroscopic ellipsometer. This work is support by Texas Instruments Distinguished Chair in Nanoelectronics. S. T. acknowledges support from VPR Post-doctoral Accelerator Award from UT Dallas. M.V. acknowledges support by the NSF UT Dallas LSAMP Bridge-to-Doctorate program (HRD 1904521).

#### References

- A. Liu, H. Zhu, H. Sun, Y. Xu, Y. Noh, Solution processed metal oxide high-κ dielectrics for emerging transistors and circuits, Adv. Mater. 30 (2018), 1706364, https://doi.org/10.1002/adma.201706364.
- [2] E. Fortunato, P. Barquinha, R. Martins, Oxide semi-conductor thin-film transistors: a review of recent advances, Adv. Mater. 24 (2012) 2945–2986, https://doi.org/ 10.1002/adma.201103228.
- [3] C.J. Brinker, G.W. Scherer, Sol-Gel Science: The Physics and Chemistry of Sol-Gel Processing, Academic Press, Cambridge, MA, 1990.
- [4] T.T. Baby, S.K. Garlapati, S. Dehm, M. Häming, R. Kruk, H. Hahn, S. Dasgupta, A general route toward complete room temperature processing of printed and high performance oxide electronics, ACS Nano 9 (2015) 3075–3083, https://doi.org/ 10.1021/nn507326z.
- [5] J.W. Park, B.H. Kang, H.J. Kim, A review of low-temperature solution-processed metal oxide thin-film transistors for flexible electronics, Adv. Funct. Mater. 30 (2020), 1904632, https://doi.org/10.1002/adfm.201904632.
- [6] S.C. Park, D. Kim, H. Shin, D.K. Lee, X. Zhang, J. Park, J.S. Choi, Advanced photo-annealing of indium zinc oxide films for thin-film transistors using pulse UV light, J. Inform. Disp. 17 (2016) 1–7, https://doi.org/10.1080/15980316.2016.1140114.
- [7] J. Leppäniemi, K. Eiroma, H. Majumdar, A. Alastalo, Far-UV Annealed Inkjet-Printed In 2 O 3 Semiconductor Layers for Thin-Film Transistors on a Flexible Polyethylene Naphthalate Substrate, ACS Appl. Mater. Inter. 9 (2017) 8774–8782, https://doi.org/10.1021/acsami.6b14654.
- [8] E. Carlos, R. Branquinho, A. Kiazadeh, P. Barquinha, R. Martins, E. Fortunato, UV mediated photochemical treatment for low temperature oxide based TFTs, ACS Appl. Mater. Inter. 8 (2016) 31100, https://doi.org/10.1021/acsami.6b06321.
- [9] J. Hwang, K. Lee, Y. Jeong, Y.U. Lee, C. Pearson, M.C. Petty, H. Kim, UV-assisted low temperature oxide dielectric Films for TFT Applications, Adv. Mater. Interfaces 1 (2014), 1400206, https://doi.org/10.1002/admi.201400206.
- [10] T.B. Daunis, D. Barrera, G. Gutierrez-Heredia, O. Rodriguez-Lopez, J. Wang, W. E. Voit, J.W.P. Hsu, Solution-processed oxide thin film transistors on shape memory polymer enabled by photochemical self-patterning, J. Mater. Res. 33 (2018) 2454–2462, https://doi.org/10.1557/jmr.2018.296.
- [11] Y.S. Rim, H.S. Lim, H.J. Kim, Low-temperature metal-oxide thin-film transistors formed by directly photopatternable and combustible solution synthesis, ACS Appl. Mater. Inter. 5 (2013) 3565–3571, https://doi.org/10.1021/am302722h.

- [12] Y. Rim, H. Chen, Y. Liu, S. Bae, H. Kim, Y. Yang, Direct light pattern integration of low-temperature solution-processed all-oxide flexible electronics, ACS Nano 8 (2014) 9680–9686, https://doi.org/10.1021/nn504420r.
- [13] T.B. Daunis, G. Gutierrez-Heredia, O. Rodriguez-Lopez, J. Wang, W.E. Voit, J.W.P. Hsu, Solution-deposited Al2O3 dielectric towards fully-patterned thin film transistors on shape memory polymer, Proceeding of SPIE. (2017) 101051Z-101051Z-8. https://doi.org/10.1117/12.2250393.
- [14] E.A. Cochran, K.N. Woods, D.W. Johnson, C.J. Page, S.W. Boettcher, Unique chemistries of metal-nitrate precursors to form metal-oxide thin films from solution: materials for electronic and energy applications, J Mater. Chem. A 7 (2019) 24124–24149, https://doi.org/10.1039/c9ta07727h.
- [15] S. Park, K. Kim, J. Jo, S. Sung, K. Kim, W. Lee, J. Kim, H.J. Kim, G. Yi, Y. Kim, M. Yoon, S.K. Park, In-depth studies on rapid photochemical activation of various sol-gel metal oxide films for flexible transparent electronics, Adv. Funct. Mater. 25 (2015) 2807–2815. https://doi.org/10.1002/adfm.201500545.
- [16] J.-S. Heo, J.-H. Kim, J. Kim, M.-G. Kim, Y.-H. Kim, S.K. Park, Photo-chemically activated flexible metal-oxide transistors and circuits using low impurity aqueous system, IEEE Electr Device L 36 (2015) 162–164, https://doi.org/10.1109/ lod/2014/2382136
- [17] Y.-H. Kim, J.-S. Heo, T.-H. Kim, S. Park, M.-H. Yoon, J. Kim, M.S. Oh, G.-R. Yi, Y.-Y. Noh, S.K. Park, Flexible metal-oxide devices made by room-temperature photochemical activation of sol-gel films, Nature 489 (2012) 128, https://doi.org/10.1038/nature11434.
- [18] T.B. Daunis, J.M.H. Tran, J.W.P. Hsu, Effects of environmental water absorption by solution-deposited Al 2 O 3 gate dielectrics on thin film transistor performance and mobility, ACS Appl. Mater. Inter. 10 (2018) 39435–39440, https://doi.org/ 10.1021/acsami.8b15592.
- [19] Y.-J. Kim, J.-K. Jeong, J.-H. Park, B.-J. Jeong, H.-D. Lee, G.-W. Lee, Selective UV–O3 treatment for indium zinc oxide thin film transistors with solution-based multiple active layer, Jpn. J. Appl. Phys. 57 (2018) 06KB01, https://doi.org/ 10.7567/jjap.57.06kb01.
- [20] K. Zhao, Y. Gong, L. Yan, W. He, D. Wang, J. Wang, Z. Zou, C. Luo, A. Zhang, Z. Fan, J. Gao, H. Ning, G. Zhou, X. Lu, J. Liu, Room-Temperature Fabrication of High-Quality Lanthanum Oxide High-κ Dielectric films by a solution process for low-power soft electronics, Adv. Electron. Mater. 5 (2019), 1900427, https://doi.org/10.1002/aelm.201900427.
- [21] G. Lavareda, C.N. de Carvalho, E. Fortunato, A.R. Ramos, E. Alves, O. Conde, A. Amaral, Transparent thin film transistors based on indium oxide semiconductor, J. Non-Cryst. Solids 352 (2006) 2311–2314, https://doi.org/10.1016/j. inoncrysol.2006.03.031.
- [22] H.S. Kim, P.D. Byrne, A. Facchetti, T.J. Marks, High performance solution-processed indium oxide thin-film transistors, J. Am. Chem. Soc. 130 (2008) 12580–12581, https://doi.org/10.1021/ja804262z.
- [23] R.A. John, N.A. Chien, S. Shukla, N. Tiwari, C. Shi, N.G. Ing, N. Mathews, Low-temperature chemical transformations for high-performance solution-processed oxide transistors, Chem. Mater. 28 (2016) 8305–8313, https://doi.org/10.1021/acs.chemmater.6b03499.
- [24] Y.M. Park, J. Daniel, M. Heeney, A. Salleo, Room-Temperature fabrication of ultrathin oxide gate dielectrics for low-voltage operation of organic field-effect transistors, Adv. Mater. 23 (2011) 971–974, https://doi.org/10.1002/ adma.201003641
- [25] I. Bretos, R. Jiménez, J. Ricote, M.L. Calzada, Photochemistry in the low-temperature processing of metal oxide thin films by solution methods, Chem. Eur. J. 26 (2020) 9277–9291, https://doi.org/10.1002/chem.202000244.
- [26] J.H. Park, Y.B. Yoo, K.H. Lee, W.S. Jang, J.Y. Oh, S.S. Chae, H.W. Lee, S.W. Han, H. K. Baik, Boron-Doped Peroxo-Zirconium Oxide Dielectric for high-performance, low-temperature, solution-processed indium oxide thin-film transistor, ACS Appl. Mater. Inter. 5 (2013) 8067–8075, https://doi.org/10.1021/am402153g.
- [27] A. Bertoluzza, C. Fagnano, M.A. Morelli, V. Gottardi, M. Guglielmi, Raman and infrared spectra on silica gel evolving toward glass, J. Non-Cryst. Solids 48 (1982) 117–128, https://doi.org/10.1016/0022-3093(82)90250-2.
- [28] S. Goldstein, J. Rabani, Mechanism of nitrite formation by nitrate photolysis in aqueous solutions: the role of peroxynitrite, nitrogen dioxide, and Hydroxyl Radical, J. Am. Chem. Soc. 129 (2007) 10597–10601, https://doi.org/10.1021/ ion73609.
- [29] J. Mack, J.R. Bolton, Photochemistry of nitrite and nitrate in aqueous solution: a review, J. Photochem. Photobiol. Chem. 128 (1999) 1–13, https://doi.org/ 10.1016/s1010-6030(99)00155-0.
- [30] N.S. Bayliss, R.B. Bucat, The photolysis of aqueous nitrate solutions, Aust. J. Chem. 28 (1975) 1965–1978, https://doi.org/10.1071/ch9751865.
- [31] M.-G. Kim, M.G. Kanatzidis, A. Facchetti, T.J. Marks, Low-temperature fabrication of high-performance metal oxide thin-film electronics via combustion processing, Nat. Mater. 10 (2011) 382, https://doi.org/10.1038/nmat3011.
- [32] W.M. Haynes, CRC Handbook of Chemistry and Physics, 91st Edition, CRC Press, 2010.